NASA Contractor Report 194449
AIAA–94–0138

Unsteady Jet Flow Computation Towards Noise Prediction

Woo-Yung Soh
Sverdrup Technology, Inc.
Lewis Research Center Group
Brook Park, Ohio

January 1994

Prepared for
Lewis Research Center
Under Contract NAS3–25266

NASA
National Aeronautics and Space Administration

Unsteady Jet Flow Computation Towards Noise Prediction

Woo-Yung Soh
Sverdrup Technology, Inc.
Lewis Research Center Group
Brook Park, Ohio 44142

Abstract

An attempt has been made to combine a wave solution method and an unsteady flow computation to produce an integrated aeroacoustic code to predict far-field jet noise. An axisymmetric subsonic jet is considered for this purpose. A fourth order space accurate Pade compact scheme is used for the unsteady Navier-Stokes solution. A Kirchhoff surface integral for the wave equation is employed through the use of an imaginary surface which is a circular cylinder enclosing the jet at a distance. Information such as pressure and its time and normal derivatives is provided on the surface. The sound prediction is performed side by side with the jet flow computation. Retarded time is also taken into consideration since the cylinder body is not acoustically compact. The far-field sound pressure has the directivity and spectra show that low frequency peaks shift toward higher frequency region as the observation angle increases from the jet flow axis.

Introduction

Jet noise suppression has appeared as a critical issue for the viability of future supersonic flight. The FAR 36 Stage III imposes the same noise limitation on future supersonic commercial flight as it does on subsonic aircraft. This brings forth a challenging task to reduce the jet noise in the High Speed Civil Transport Program. In order to accomplish this task, assessment of far-field noise generated by a jet plume is a prerequisite to the design of the engine. Jet noise is generated as a byproduct of the plume flow behind the exhaust nozzle. Flow turbulence has been believed to be a source of the sound. Lighthill[1] showed that the flow turbulence, which is referred to as the fluctuating Reynolds stress or Lighthill's tensor, is the sound source. Since then, turbulent flow, which had been generally accepted as a totally chaotic entity, has been a central theme in the aeroacoustic research. For an estimation of the sound pressure using the acoustic analogy approach, the two-point fourth order correlation of the fluctuating Reynolds stress must be computed. To make this tractable, Proudman[2] pursued a noise generation theory that assumes the isentropic turbulence. A variety of manipulation and modelling of the flow turbulence has been made based on a fully turbulent assumption since then.

Freymuth[3] observed organized large eddy structures in a separated flow of a jet. Brown and Roshko[4] also found large vortical structures in a free shear layer. These findings of the vortical pattern in the free shear layer filled the gap between an initial wave region, in which a linear theory is applied, and the fully turbulent downstream region. The flow regime dominated by the large vortical structure is not fully random and is predictable in a deterministic way. This organized structure maintains its identity up to the point where the potential core begins to collapse but is still discernable even in the fully turbulent region far downstream. Winant and Browand[5] reported that a mechanism of the mixing layer growth is an interaction of adjacent large vortices. These investigators have shown that the flow in free shear layers such as jet and plane mixing flow is well behaved and more organized than previously thought. Shear flow is dominated by large vortical structures, which are very predictable and controllable. This shear flow, which had been thought to be fully turbulent and therefore random and chaotic, has become research subject with a quite different perspective since the observation of these organized structures. A decomposition of the fluctuating flow quantity into the organized flow entity and the fully random entity makes it possible to study turbulent shear flows in a certain deterministic way.

Experiments[6] have shown that the sound power emitted from the jet column is greatest within 4 or 5 diameters downstream, and then decays rapidly through a transition region. This indicates that the initial development of the jet, before it becomes fully turbulent, should be clearly resolved so that an accurate noise prediction can be made. This region is characterized by large vortical structures and is not fully turbulent, which gives the motivation that we solve the unsteady flow equation directly to provide the sound source for an acoustic computation of the far-field noise. Numerical solution of turbulent flow is difficult because the turbulent flow field is made up of a range of length scales from the Kolmogorov scale to the integral scale. If numerical mesh size can be made fine enough to resolve the smallest scales which dissipate the kinetic energy, then direct numerical simulation (DNS) is the tool to obtain the entire turbulent flow structure. However, the dissipative scale becomes finer as the Reynolds number is increased and practical hardware limitations are rapidly reached. Therefore, the DNS method is limited to simulating only low Reynolds number turbulence. For practical computation of higher Reynolds number flows, small scale fluctuations can be

modeled so that desired large scale eddies can be computed directly, while proper dissipation is provided by the small scale eddy model. This approach, which is referred to as large eddy simulation (LES), has been successfully employed in many flows with practical applications.

In order to obtain the flow field as the source of sound using DNS or LES, the simulations must be performed using numerical techniques with minimal distortion and diffusive characteristics. The source of numerical diffusion and phase error is known to be mainly from the numerical formulation of the convective terms. These numerical artifacts get worse for high Reynolds number flow simulations. Typically, free shear flows of interest have very high Reynolds numbers. Therefore, a higher order accurate numerical scheme which meets the previously mentioned requirements is needed. Fourth order Pade compact differencing scheme with a dispersion relation preserving property is used here.

It is the purpose of this paper to present a method to predict the far-field pressure directly from the numerically generated unsteady flow solution without recourse to empirical factors. Therefore, only an axisymmetric laminar jet is considered in the process of incorporating a wave solution into the higher order accurate flow solver. Furthermore, the flow solution is limited to the subsonic case since supersonic jets often generate shock related noise in addition to the shear noise due to flow turbulence, which makes the problem more complicated. The Kirchhoff surface integral method is chosen for the solution of the wave equation. The acoustic result obtained is the far-field sound caused by the wavy motion and large vortical structure of the free shear layer. Fine scale random turbulence is not addressed in this study.

Governing Equation of Fluid Flow

The variables $T, \rho, \mathbf{x}, \mathbf{u}, t, p$, and e are dimensionless quantities of temperature, density, position, velocity, time, pressure, and total energy per unit mass based on reference quantities $T_r^*, \rho_r^*, l_r^*, u_r^*, t_r^*, p_r^*$ and e_r^*, respectively. Additional definitions are $t_r^* = l_r/u_r, p_r^* = \rho_r u_r^2$, and $e_r^* = u_r^2$. Then the equation of state becomes the following:

$$p = \frac{\rho T}{\gamma M_r^2} \quad \text{with} \quad T = \gamma(\gamma-1)M_r^2\left(e - \frac{u^2+v^2}{2}\right)$$

where γ is the ratio of specific heats, $M_r = u_r^*/\sqrt{\gamma R T_r^*}$, here R is the gas constant. The Navier-Stokes equations for axisymmetric flow in the cylindrical coordinates (x, r) are written as :

$$\frac{\partial \mathbf{q}}{\partial t} + \frac{\partial \mathbf{f}}{\partial x} + \frac{\partial \mathbf{g}}{\partial r} = \mathbf{s} \quad \text{where} \quad \mathbf{q} = (\rho, \rho u, \rho v, \rho e)^T \quad (1)$$

$$\mathbf{f} = \begin{pmatrix} \rho u \\ \rho u^2 + p - \frac{\mu}{Re}\tau_{xx} \\ \rho uv - \frac{\mu}{Re}\tau_{xr} \\ (\rho e + p)u - \frac{\mu}{Re}(\tau_{xx}u + \tau_{xr}v) - \frac{k}{(\gamma-1)RePrM_r^2}\frac{\partial T}{\partial x} \end{pmatrix}$$

$$\mathbf{g} = \begin{pmatrix} \rho v \\ \rho uv - \frac{\mu}{Re}\tau_{xr} \\ \rho v^2 + p - \frac{\mu}{Re}\tau_{rr} \\ (\rho e + p)v - \frac{\mu}{Re}(\tau_{xr}u + \tau_{rr}v) - \frac{k}{(\gamma-1)RePrM_r^2}\frac{\partial T}{\partial r} \end{pmatrix}$$

where superscript T is the transpose of the matrix, (u, v) are the velocities in (x, r), and the source term s and stress tensors are defined as:

$$\mathbf{s} = -\frac{1}{r}\left[\mathbf{g} + (0, 0, p - \tau_{\phi\phi}, 0)^T\right]$$

$$\tau_{xx} = \lambda\nabla\cdot\mathbf{u} + 2\mu\frac{\partial u}{\partial x}, \quad \tau_{rr} = \lambda\nabla\cdot\mathbf{u} + 2\mu\frac{\partial v}{\partial r},$$

$$\tau_{xr} = \mu\left(\frac{\partial u}{\partial r} + \frac{\partial v}{\partial x}\right), \quad \tau_{\phi\phi} = \lambda\nabla\cdot\mathbf{u} + 2\mu\frac{v}{r}$$

Heat conductivity k and viscosity μ are scaled by k_r^* and μ_r^*, which are the values at T_r^*. The second viscosity λ is $-\frac{2}{3}\mu$. Dimensionless numbers, Re and Pr, are the Reynolds and Prandtl numbers defined to be $\rho_r^* u_r^* l_r^*/\mu_r^*$ and $\mu_r^* c_p/k_r^*$, respectively. The dimensionless speed of sound c becomes $\sqrt{T}/M_r$. Equation (1) is written in generalized coordinates ξ and η as:

$$\frac{\partial \mathbf{Q}}{\partial t} + \frac{\partial \mathbf{F}}{\partial \xi} + \frac{\partial \mathbf{G}}{\partial \eta} = \mathbf{S} \quad \text{where} \quad \mathbf{Q} = J\mathbf{q}, \quad \mathbf{S} = J\mathbf{s} \quad (2)$$

$$J = (\xi_x\eta_r - \xi_r\eta_x)^{-1}, \ \mathbf{F} = J(\xi_x\mathbf{f} + \xi_r\mathbf{g}), \ \mathbf{G} = J(\eta_x\mathbf{f} + \eta_r\mathbf{g})$$

Formulation of Difference Scheme

To obtain a first derivative of $f(x)$, a Pade compact differencing[7,8,9] is formulated as :

$$\alpha f'_{i-1} + f'_i + \alpha f'_{i+1} = b\frac{f_{i+2} - f_{i-2}}{4h} + a\frac{f_{i+1} - f_{i-1}}{2h} \quad (3)$$

where h is the mesh size. If we use the truncated Taylor series to make equation (3) a fourth order approximation, the values of a and b are :

$$a = \frac{2\alpha + 4}{3} \qquad \text{and} \qquad b = \frac{4\alpha - 1}{3}$$

Equation (3) can render a sixth order accuracy if α is set to $\frac{1}{3}$. In a general fourth order formulation, α is a free parameter and it will be optimized by the dispersion relation preserving concept proposed by Tam and Webb[10] as described below. Fourier transform of $f(x)$ and its inverse are defined as :

$$\tilde{f}(w) = \frac{1}{\sqrt{2\pi}} \int_{-\infty}^{+\infty} f(x) e^{-iwx}\, dx$$

$$f(x) = \frac{1}{\sqrt{2\pi}} \int_{-\infty}^{+\infty} \tilde{f}(w) e^{iwx}\, dw$$

Fourier transforming equation (3) by the above definition gives :

$$i(1 + 2\alpha \cos\kappa)\tilde{f}(w) = i\,(a \sin\kappa + \frac{b}{2}\sin 2\kappa)\tilde{f}(w)$$

This expression indicates that the wave number is deformed by our discretization process into a different wave number as :

$$\tilde{\kappa} = \frac{a \sin\kappa + \frac{b}{2}\sin 2\kappa}{1 + 2\alpha \cos\kappa} \qquad (4)$$

where κ is the input wave number defined to be wh and $\tilde{\kappa}$ the deformed response wave number. In reference [10] the optimum α is chosen so that the following function K is minimized. (i.e $\partial K/\partial\alpha = 0$)

$$K = \int_{-\pi/2}^{\pi/2} (\kappa - \tilde{\kappa})^2\, d\kappa$$

The optimum value of α is computed to be 0.35619. Figure 1 shows the wave relation. The straight line is for the exact derivative. It is also found that the fourth order approximation with the optimum value of α has better wave performance than the sixth order approximation in the most compact form.

The four-stage Runge-Kutta technique[11] is adopted for an explicit time advancement formulation. To obtain new flow variables at $t = (n+1)\Delta t$ from known data at $t = n\Delta t$, equation (2) is used to advance the solution in time as follows :

$$\mathbf{Q}^{(1)} - \mathbf{Q}^n = \alpha_1\, \Delta t \mathbf{W}^{(0)}$$

$$\mathbf{Q}^{(2)} - \mathbf{Q}^n = \alpha_2\, \Delta t \mathbf{W}^{(1)}$$

$$\mathbf{Q}^{(3)} - \mathbf{Q}^n = \alpha_3\, \Delta t \mathbf{W}^{(2)}$$

$$\mathbf{Q}^{(4)} - \mathbf{Q}^n = \alpha_4\, \Delta t \mathbf{W}^{(3)} + \mathbf{D}$$

where $\mathbf{W}^{(k)}$ denotes $\mathbf{S} - \partial\mathbf{F}/\partial\xi - \partial\mathbf{G}/\partial\eta$ evaluated at the k-th stage. The stage 0 and 4 are at the time, $n\Delta t$ and $(n+1)\Delta t$. The parameters, $\alpha_1, \alpha_2, \alpha_3, \alpha_4$, are given to be $\frac{1}{4}, \frac{1}{3}, \frac{1}{2}, 1$. This time difference is second order accurate and the intermediate variables are not stored at every stage.

A numerical dissipation term $\mathbf{D}$ is added during the fourth stage to enhance the numerical stability. The dissipation term is introduced to be of sixth order so that our fourth order accuracy remains intact.

$$\mathbf{D} = \omega_e J\left(\frac{\partial^6 \mathbf{q}}{\partial\xi^6} + \frac{\partial^6 \mathbf{q}}{\partial\eta^6}\right)$$

where ω_e is a constant and $\partial^6\mathbf{q}/\partial\xi^6$ is given by :

$$\frac{\partial^6 \mathbf{q}}{\partial\xi^6} = 15(\mathbf{q}_{i+1j} + \mathbf{q}_{i-1j}) - 6(\mathbf{q}_{i+2j} + \mathbf{q}_{i-2j}) + (\mathbf{q}_{i+3j} + \mathbf{q}_{i-3j}) - 20\mathbf{q}_{ij}$$

The derivative $\partial^6\mathbf{q}/\partial\eta^6$ in the η direction is obtained in the similar manner. This numerical dissipation is applied to internal points.

Boundary Condition

The boundary treatment considered here is a combination of characteristic and algebraic boundary conditions. The characteristic boundary condition solves the governing equation in a characteristic form in each coordinate direction and the algebraic boundary conditions are the given boundary conditions such as temperature, total temperature, velocity, *etc.* Equation (2) is written in a non-conservative form as:

$$\frac{\partial \mathbf{q}}{\partial t} + \mathbf{A}\frac{\partial \mathbf{q}}{\partial \xi} + \mathbf{B}\frac{\partial \mathbf{q}}{\partial \eta} = \mathbf{s}_r$$

where $\mathbf{s}_r = r^{-1}(\eta_x\mathbf{F} - \xi_x\mathbf{G} + \mathbf{s}), \mathbf{A} = \partial\mathbf{F}_i/\partial\mathbf{q}, \mathbf{B} = \partial\mathbf{G}_i/\partial\mathbf{q}$, and the subscript i denotes the inviscid part. For the ξ direction, equation (2) with a transformation $d\mathbf{q} = \mathbf{R}_\xi d\tilde{\mathbf{q}}$ becomes

$$\frac{\partial \tilde{\mathbf{q}}}{\partial t} + \mathbf{R}_\xi^{-1}\mathbf{A}\mathbf{R}_\xi\frac{\partial \tilde{\mathbf{q}}}{\partial \xi} + \mathbf{R}_\xi^{-1}\mathbf{B}\mathbf{R}_\xi\frac{\partial \tilde{\mathbf{q}}}{\partial \eta} = 0$$

If we construct the matrix $\mathbf{R}_\xi$ such that the eigenvectors of the matrix $\mathbf{A}$ constitute its columns then the matrix by a similarity transform becomes a diagonal matrix, whose entries are the eigenvalues of $\mathbf{A}$ such that

$$\mathbf{R}_\xi^{-1}\mathbf{A}\mathbf{R}_\xi = \mathbf{\Lambda}_\xi = \mathrm{diag}(U, U, U + a_\xi, U - a_\xi)$$

where $a_\xi = c\sqrt{\xi_x^2 + \xi_y^2}$. Here, c is the speed of sound defined to be $\sqrt{T}/M_r$, and $U = \xi_x u + \xi_y v$. In the same way, for the η direction the diagonal matrix becomes :

$$\mathbf{R}_\eta^{-1}\mathbf{B}\mathbf{R}_\eta = \mathbf{\Lambda}_\eta = \mathrm{diag}(V, V, V + a_\eta, V - a_\eta)$$

where $a_\eta = c\sqrt{\eta_x^2 + \eta_y^2}$, and $V = \eta_x u + \eta_y v$. The characteristic equations are then rewritten in each coordinate direction to be:

$$\mathbf{R}_\xi^{-1}\frac{\partial \mathbf{q}}{\partial t} + \mathbf{\Lambda}_\xi \mathbf{R}_\xi^{-1}\frac{\partial \mathbf{q}}{\partial \xi} + \frac{\mathbf{R}_\xi^{-1}}{J}\frac{\partial \mathbf{G}}{\partial \eta} = \mathbf{R}_\xi^{-1}\mathbf{s}_r \qquad (5)$$

$$\mathbf{R}_\eta^{-1}\frac{\partial \mathbf{q}}{\partial t} + \mathbf{\Lambda}_\eta \mathbf{R}_\eta^{-1}\frac{\partial \mathbf{q}}{\partial \eta} + \frac{\mathbf{R}_\xi^{-1}}{J}\frac{\partial \mathbf{F}}{\partial \xi} = \mathbf{R}_\eta^{-1}\mathbf{s}_r \qquad (6)$$

Nonreflecting boundary conditions[12,13] can be constructed by setting any eigenvalue, which is the element of $\mathbf{\Lambda}$, to be zero, if a wave is incoming towards the computational domain.

Jet Flow Calculation

The subsonic jet Mach number is 0.6 and the ambient air is at M=0.2 and the two streams are brought to be mixed at the same temperature. The reference length l_r^* is taken to be the nozzle radius R. u_r^* is the average velocity of the two streams and M_r is the average Mach number of the two streams. Since the temperature variation is assumed small over the entire flow domain the viscosity and the heat conductivity are held constant at the reference temperature $T_r^* = 298°K$. The inlet boundary conditions are given by :

$$u = 1 - \lambda_s \tanh(20(r-1)),\ v = 0,\ T = 1 \qquad (7)$$

and there is one characteristic equation for the outgoing wave. The shear ratio λ_s is defined to be $\Delta u^*/u_r^*$, where Δu^* is the velocity difference in the two streams. The characteristic boundary conditions at the exit and side boundary planes are given as described in equations (5) and (6). As to initial condition, u has the above tanh profile, $v = 0$, $T = 1$, $\rho = 1$, $p = (\gamma M_r^2)^{-1}$. The Reynolds and Prandtl numbers are 174000 and 0.707, respectively. The nozzle radius R, which is the reference length l_r^*, is taken to be 1.95 cm.

A 600 × 160 stretched grid, which extends up to about 59.3 and 9.2 radii in the respective axial and radial directions, is used. Figure 2, drawn at every fourth grid line, shows the grid clustered near the nozzle height. Instantaneous contour plots of the vorticity, Mach number, and static pressure are presented in Figure 3. These clearly indicate a large vortical structure in the developing jet flow. Local pressure minima coincide with the centers of vortices. Figure 4 is the time sequence of the vorticity of the jet. Each frame of the contour plots is $100\Delta t$ apart. The flow structure is wavy yet well connected in the early stage of the flow development region. This wave motion is magnified and the confined vorticity layer rolls up to form a discrete vortex lump, which can be seen in every frame of vorticity contour. This vortex roll-up is followed by vortex shedding and vortex pairing as the flow proceeds downstream. The vortex pairing is the coalescence process of two consecutive vortices and is known as the shear layer growth mechanism. The convective velocity with which the large vortical structure moves is obtained to be 1.06 from Figure 4, which is very close to the mean velociy of the two streams. The convective velocity is constant regardless of the location and size of the vortex. The only exception is when the vortex pairing takes place where the vortex which travels behind the preceeding one speeds up to catch up with the latter and the two slide on each other to coalese into a larger one. The convective velocity obtained by the present computation agrees very well with the expressions given by Dimotakis[14] and Papamoschou and Roshko[15]. They assumed that the dynamic pressure of the two streams should be about the same in the frame which moves with the convective velocity.

Figure 5 shows the axial velocity spectra. The abscissa is $St(D)$, the Strouhal number defined to be fD/U_j with U_j the jet center velocity at the nozzle exit and the ordinate represents the absolute value of Fourier coefficient. D is the diameter of the nozzle. The most preferred frequency of $St(D)$=0.63, which appears dominant at the upstream region, persist up to x=4D in Figure 5. This dominant high frequency shifts towards the low frequency and the spectra show the single most dominant frequency of about $St(D)$=0.35 from the downstream of x=6D. This frequency is close to the average Strouhal number of 0.3 based on the downstream puff counts by Crow and Champagne[16]. Many experiments have confirmed that the $St(D)$ of about 0.3 is the dominant frequency of the organized vortical structure where the potential core ceases to exist.

Peaks in the power spectra of the u velocity show the most preferred frequencies : $St(\theta)$=0.006 at x=$D/2$ and D, $St(\theta)$=0.021 at x=2D, $St(\theta)$=0.022 at x=3D, and $St(\theta)$=0.034 at x=4D. This Strouhal number is defined to be $f\theta/U_j$ with θ the local momentum thickness defined as :

$$\theta = \frac{1}{\Delta U^2}\int_0^\infty (U - U_s)(U_f - U)\,dr \qquad (8)$$

$St(\theta)$ is the most frequently used flow parameter in describing initial flow development. According to the linear theory by Michalke[17], the most amplified $St(\theta)$ is about 0.017 for a spatially evolving jet flow with a hyperbolic tangent mean velocity profile. The linear theory agrees with Freymuth's experiment[3] up to about $St(\theta)$=0.01, but experiment exhibits a flat peak area over $0.01 \le St(\theta) \le 0.025$. Considering a flow region in which flow solution adjust itself from a boundary condition to a flow solution, the computed Strouhal number of about 0.02, which is most preferred at x=2D and 3D, is close to both the theory and the experiment.

The mean axial velocity profiles are given in Figure 6. The potential core in the middle erodes as flow proceeds downstream and vanishes as shown at x=8D. Further downstream the mean velocity profile maintains the same profile as at x=8D rather than undergoing rapid decay. This is a huge departure from the experimental observation. Figure 7 also shows the profiles of $u_{\rm rms}$. The growth of $u_{\rm rms}$ at the nozzle height (i.e. r=1) is shown in Figure 8. Both natural and forced cases are presented. Forcing is given at the most preferred upstream $St(D)$ of 0.63 and its subharmonic 0.315. $u_{\rm rms}$ becomes saturated at about 0.3 for all three cases. The maximum of $u_{\rm rms}$ grows up to about 0.3 and never decays far downstream. An Euler computation shows essentially the same results as the viscous computation. This is because our viscous computations do not include an adequate device dissipating turbulence energy due to small scale random motion.

Far-field Sound Prediction

As mentioned earlier, the flow field as simulated will be used as the sound source. There are two main ways to predict far-field noise from the numerical flow solution. The first approach is the acoustic analogy. According to Lighthill's acoustic analogy, the wave equation for static pressure p can be obtained as :

$$\frac{\partial^2 p}{\partial t^2} - a_0^2 \frac{\partial^2 p}{\partial x_i^2} = a_0^2 \frac{\partial^2}{\partial x_i \partial x_j}(\rho u_i u_j - \tau_{ij}) \qquad (9)$$

where a_0 is the reference ambient speed of sound. A deviation from an isentropic state, which is $\partial^2(p - a_0^2\rho)/\partial t^2$, is neglected in equation (9). The source term in the right-hand-side of the above equation is of quadrupole type. If the source term is assumed *a priori* known and physical obstacles are not present, the solution of equation (9) is given by a volume integral as :

$$p(\mathbf{x},t) - p_0 = \frac{1}{4\pi}\int_V \frac{1}{r}[q]^*\, dV(\mathbf{y}) \qquad (10)$$

where $r = |\mathbf{x} - \mathbf{y}|$, p_0 is the undisturbed pressure, q the source terms in equation (9) and the quantity in $[\,]^*$ is defined as :

$$[q]^* = q(\mathbf{y}, t^+) = q\left(\mathbf{y}, t - \frac{r}{a_0}\right)$$

t^+ is called the retarded time, which is the emission time for a acoustic signal to travel from the source point $\mathbf{y}$ to the field point $\mathbf{x}$. Figure 9-(a) shows the geometric variables used in the above definition. P($\mathbf{x}$) is the field point where p is being sought and Q($\mathbf{y}$) is the source point. More details of the acoustic analogy method can be found in Fuchs and Michalke[18]. Direct computation of the far-field sound by the acoustic analogy from the unsteady flow solution can be found in the references[19,20]. The acoustic analogy is a useful method to predict a far-field pressure. However, because it uses the wave equation as a governing equation even in the flow region where all kinds of nonlinear interactions occur, the solution omits important wave phenomena such as the refraction due to shear and the doppler effect by movement of the source element.

If the wave phenomenon is separable from the fluid dynamics, the wave equation can be solved to take into account all the physical effects. Let us imagine that away from the flow area there is a region where flow fluctuation is negligible so that a pure acoustic field assumption is valid. In this case, the flow and the acoustic regions can be separated and the flow equation and the wave equation can be solved side by side in their respective regions. Acoustic information is transfered from the flow solution on the boundary joining the two regions. This surface away from a flow regime is illustrated in Figure 9-(b). If all the necessary pressure information is provided on the surface, the pressure at $\mathbf{x}$ can be given by the Kirchhoff surface integral form as :

$$p(\mathbf{x},t) - p_0 = \frac{1}{4\pi}\int_A \{\frac{1}{r}[\frac{\partial p}{\partial n}]^* + \frac{1}{r^2}\frac{\partial r}{\partial n}[p]^* + \frac{1}{a_0 r}\frac{\partial r}{\partial n}[\frac{\partial p}{\partial t}]^*\}\, dA(\mathbf{y}) \qquad (11)$$

where $[\,]^*$ has the same definition as before and $\mathbf{n}$ the unit normal to the surface. Equation (11) is the solution of the wave equation for the acoustic medium at rest. The necessary information includes the pressure and its normal and time derivatives on the surface.

Wave Solution Example

A pressure wave, which is generated by a simple monopole source and radiated spherically, has been chosen as an example problem to demonstrate the surface integral method given by equation (11). The pressure satisfying a homogeneous form of the wave equation (9) can be written as :

$$p - p_o = \sin 2\pi(r - t)/r \qquad (12)$$

Length and time are nondimensionalized by wave length λ and inverse of frequency f^{-1}. We now choose a cylinder surface as an arbitrary boundary surface on which the histories of p, p_n, p_t are provided. This is shown in Figure 10. The source is located at the origin. The cylinder radius is 0.5 and length is unity, so the cylinder is not acoustically compact. For a spatial resolution in the surface integral, Δx and Δr are taken to be $\frac{1}{30}$. Circumferntial elements are set to be 100 on the side and two lid surfaces of the cylinder. For retarded time consideration, a complete set of pressure information over

an entire time period is needed. Far-field points, which are observation points, are located 10° apart at a distance $r = 50\lambda$ as shown in Figure 10. Only angles from 0° to 90° are considered due to symmetry. Figure 11 plots the sound pressure (i.e. $p_{\rm rms}$) against observation angle and shows how crucial it is to resolve the retarded time. Exact value of the $p_{\rm rms}$ for this example is 0.01414 with no preferred directivity. $p_{\rm rms}$ obtained by employing 40 time elements is almost the same as the exact solution. Figure 12-(a) also shows the time history of the pressure at angles 0° and 90°. The two curves show little difference when 40 time segments are used in resolving a time period. It can be concluded that a proper resolution of the retarded time is essential to get the correct wave characteristics. Figure 12-(b) is for an instantaneous pressure against distance which decays as r^{-1}. Two curves at 0° and 90° are identical with 40 time elements per period.

If the source has multiple frequency contents, the refinement of the retarded time is increasingly important since the highest frequency of interest should be adequately resolved. Likewise, the spatial refinement also becomes important. Therefore, for wave propagation, which is generated by a distributed source with frequencies varying over a broad range, refinement of surface elements should be emphasised as well.

Far-Field Sound Generated by Unsteady Jet Flow

Figure 13 gives the schematics of the surface on which the pressure information is specified and the field positions where the noise is observed. A cylinder is chosen to accomodate a jet column. The radius of the cylinder is about $4R$ and the length is about $20R$. The observation points are on the plane comprising the axis of jet center spacing 10° apart circumferentially at distances of $200R$ and $400R$. For the frequency of about $St(D)$=0.3, which is fluid dynamically dominant downstream, an acoustic wave length can be estimated to be about 11 for the jet of M=0.6 speed. This length could be much shorter for the wave with upstream preferred Strouhal number. Therefore, the cylinder body chosen can not be treated as acoustically compact, so the retarded time contribution should be considered. The length of time record we have to keep track of depends on the size of the cylinder. The difference between the minimum and maximum times to transmit an acoustic signal to the observation point is about 16 (i.e. times taken for the sound to travel from A to B and from A to C). With Δt of 0.00875, 1867 time steps are needed to cover the retarded time which spreads over 16 time units. This is too long, so the acoustic computation is performed at every 3 time steps. We set $\Delta t_s = 3\Delta t$ and $630\Delta t_s$ are used to retarded time distribution in the noise computation. The Δt and Δt_s are referred to as the flow and acoustic time steps, respectively.

The cylinder surface is divided into 80 circumferential elements, but only half of them are used due to the axisymmetry. In performing the surface intergal of equation (11), a contribution by two lid surfaces is omitted and only the side surface of the cylinder is considered. 258 mesh points in the axial direction are used to form a cylinder which extends to x=$20R$ downstream with the radius of $4R$. Therefore, an additional storage of 258 × 630 for each of p, p_n, and p_t and 258 × 40 × N_o for each of r and $\partial r/\partial n$ is needed. N_o is the number of observation points, which is 19 in the present work, and 40 is the half of the circumferential elements.

The OASPL (the overall sound pressure level) at r=$200R$ and $400R$ is given in Figure 14. The computed result qualitatively agrees with the experiment by Moore[21] which revealed the maximum in the OASPL at about 20° over a variety of subsonic speed conditions. The differences are that the present OASPL has the maximum at about 10° and double-peak in 10° to 40°, whereas the experimental data shows a single peak in this area. Figure 15 shows the spectra of the pressure at r=$100D$. At 0°, peak Strouhal numbers are 0.13, 0.20, 0.28, 0.46. At 10°, peak Strouhal numbers are 0.13, 0.20, and 0.46. From the pressure spectra between 0° and 20° the dominant frequencies fall in the range of $St(D)$=0.13~ 0.28. As the angle diverges from the flow direction, the dominant peak shifts toward higher frequencies, which is Strouhal number of 0.61 briefly at 30° and of 0.46 for a broad range of angle.

Conclusion and Discussion

Far-field sound pressure has been evaluated directly from a side-by-side computation with the solution of unsteady jet flow. The OASPL has maximum directivity at about 10° from the jet flow axis. The spectra of the far-field pressure show a similar trend as the experiment in that low frequency dominates at the smaller angle from the flow axis and shifts to the higher frequency as the angle increases. Although the present results agree qualitatively with the experimental observations, the present method has the following limitations : (1) helical mode of the jet flow is excluded due to the axisymmetry assumption, which has a strong effect on the growth of the instability downstream. (2) The turbulence intensity never decays even far downstream because no adequate dissipating mechanism is provided for small scale turbulence energy. (3) The Green's funtion used in the Kirchhoff surface integral for the wave is best suited to wave propagation problems through a quiescent medium, so the surface integral is to be modified to be the solution of the convective wave equation if the surrounding fluid has some considerable flow speed.

Items (1) and (2) suggest that the flow simulation

be of LES type so that the jet flow solution can accomodate a non-axisymmetric mode and mimic a realistic decay of the jet column downstream. This would probably lead to a quantitatively more accurate noise prediction.

References

[1] M.J. Lighthill, "On sound generated aerodynamically I. General theory", *Proc.Roy.Soc.* Ser.A,**211**, 564-587, 1952.

[2] I. Proudman, "The generation of noise by isotropic turbulence", *Proc.Roy.Soc.* Ser.A, **241**, 119-132, 1952.

[3] P. Freymuth, "On transition in a separated laminar boundary layer", *J.FluidMech.* **25**, 683-704, 1966.

[4] G.L. Brown and A. Roshko, "On density effects and large structure in turbulent mixing layers", *J.FluidMech.* **64**, 775-816, 1974.

[5] C.D. Winant and F.K. Browand, "Vortex pairing mechanism of turbulent mixing-layer growth at moderate Reynolds number", *J.FluidMech.* **63**, 237-255, 1974.

[6] J.C. Laurence, " Intensity, scale and spectra of turbulence in mixing region of free subsonic jet", NACA Rep. no.1292. 1956.

[7] S.K. Lele, "Direct numerical simulation of compressible free shear flow", AIAA paper 89-0374.

[8] S.T. Yu, Y.-L.P. Tsai and K.C. Hsieh, "Runge-Kutta methods combined with compact difference schemes for the unsteady Euler equations", AIAA paper 92-3210

[9] W.Y. Soh, "Numerical Simulation of Free Shear Flows -Towards a Predictive Computational Aeroacoustics Capability", NASA CR 191015, 1993.

[10] C.K.W. Tam and J.C. Webb, "Dispersion-Relation-Preserving finite difference schemes for computational acoustics", *J.Comput.Phys.* **107** 262-281, 1993

[11] A. Jameson, W. Schmidt and E. Turkel, "Numerical solution of the Euler equations by finite volume methods using Runge-Kutta time stepping schemes", AIAA paper 81-1259.

[12] G.W. Hedstrom, "Nonreflecting boundary conditions for nonlinear hyperbolic systems", *J.Comput.Phys.*. **30**, 222-237, 1979.

[13] K.W. Thompson, "Time dependent boundary conditions for hyperbolic systems", *J.Comput.Phys.* **68**, 1-24, 1987.

[14] P.E. Dimotakis,"Entrainment into a fully developed, two-dimensional shear layer", AIAA paper 84-0368.

[15] D. Papamoschou and A. Roshko, "Observations of supersonic free shear layers", AIAA paper 86-0162.

[16] S.C. Crow and F.H. Champagne, "Orderly structure in jet turbulence", *J.FluidMech.* **48**, part 3, 547-591, 1971.

[17] A. Michalke, "On spatially growing disturbances in an inviscid shear layer", *J.FluidMech.* **23**, part 3, 521-544, 1965.

[18] H.V. Fuchs and A. Michalke, "Introduction of aerodynamic noise theory", Progress in Aerospace Sciences, Vol.14, ed. by D. Küchemann, Pergamon Press, 1973.

[19] J.C. Hardin and S.L. Lamkin,"Aeroacoustic computation of cylinder wake flow", *AIAA J.* **22**, 51-57, 1984.

[20] W.Y. Soh, "Numerical simulation of free shear flows and far-field sound pressure directivity", will appear in *Int.J.Num.Meth.Fluids*.

[21] C.J. Moore, "The role of shear-layer instability waves in jet exhaust noise", *J.FluidMech.* **80**, 321-367, 1997.

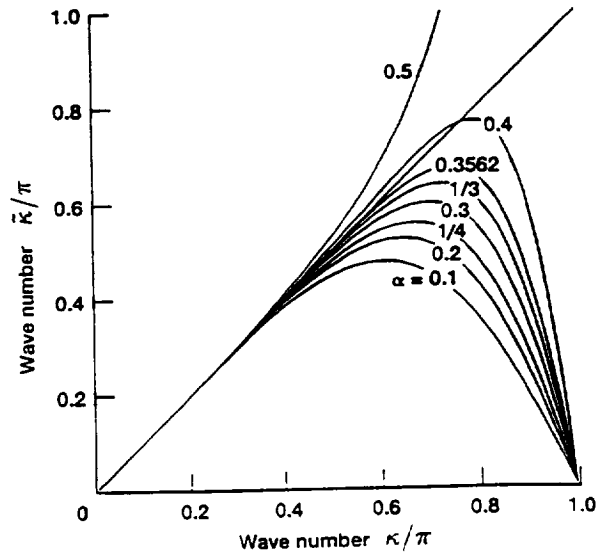

Figure 1. Wave relation given by Equation (4).

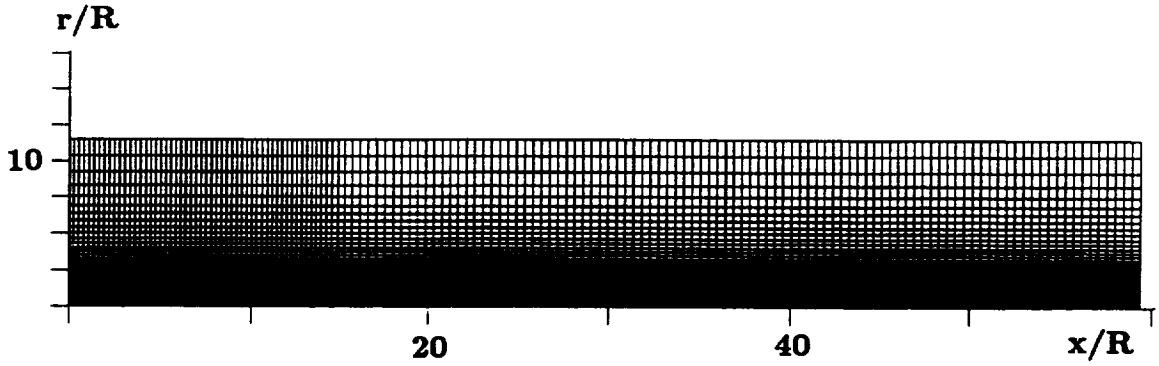

Figure 2. 600 x 160 stretched grid.

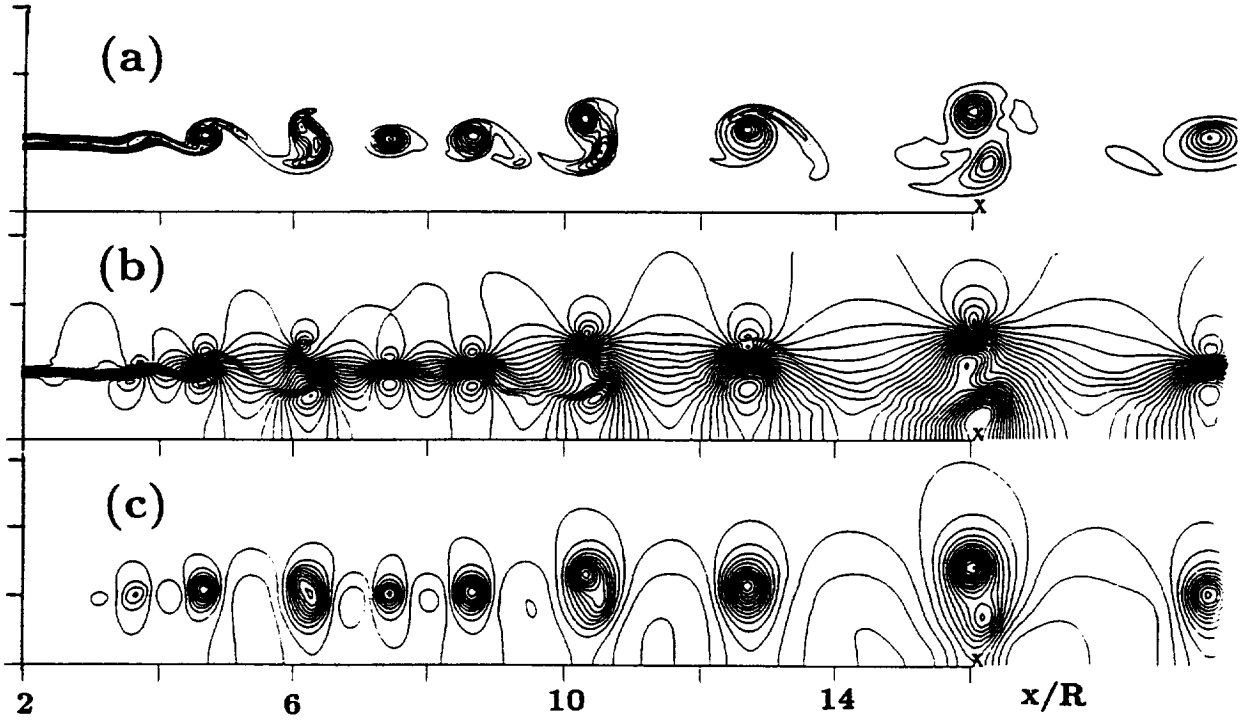

Figure 3. Contour plots of (a) vorticity, (b) Mach number, and (c) static pressure.

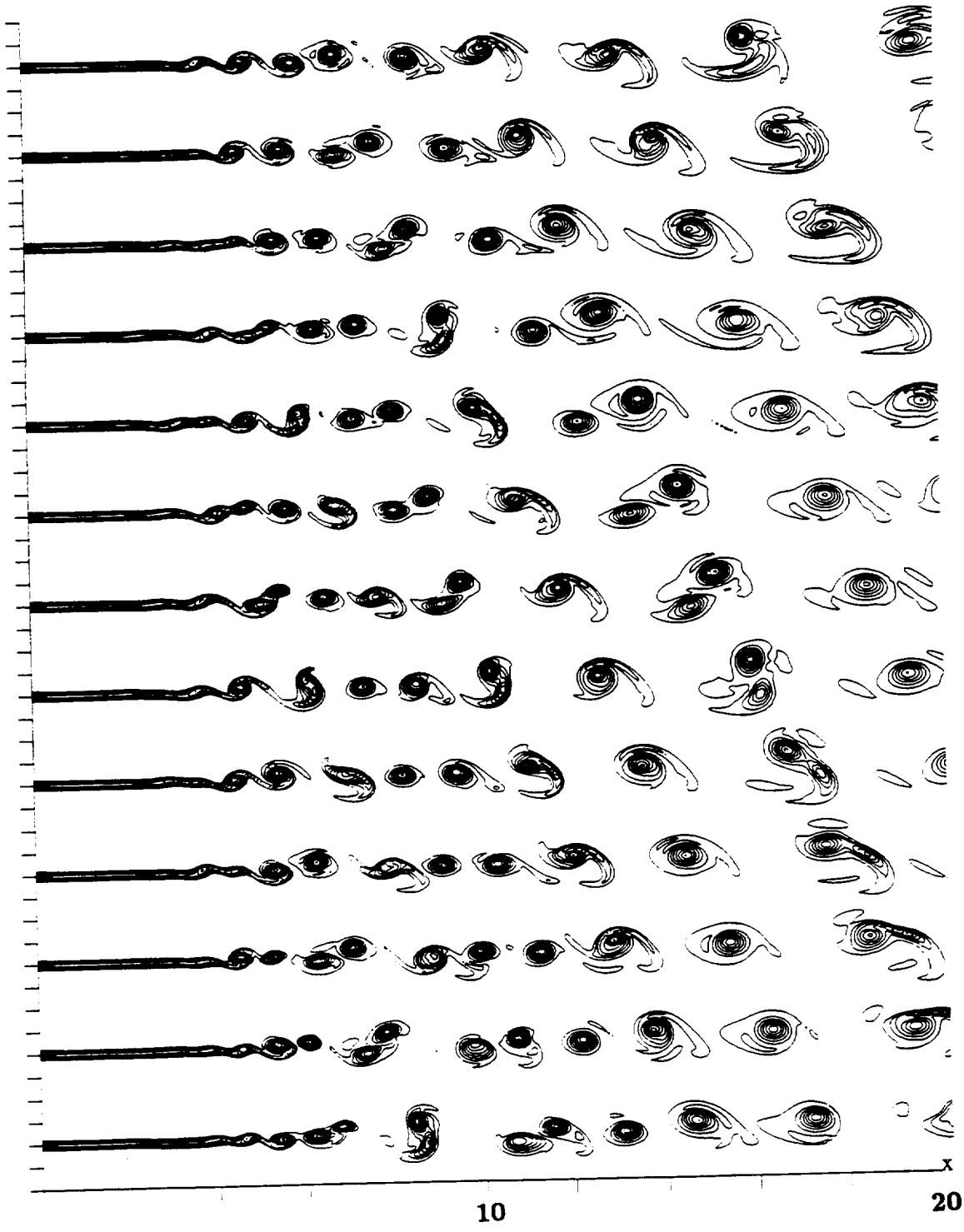

Figure 4. Vorticity contour at every $100\Delta t$ computed by Pade scheme with optimum α.

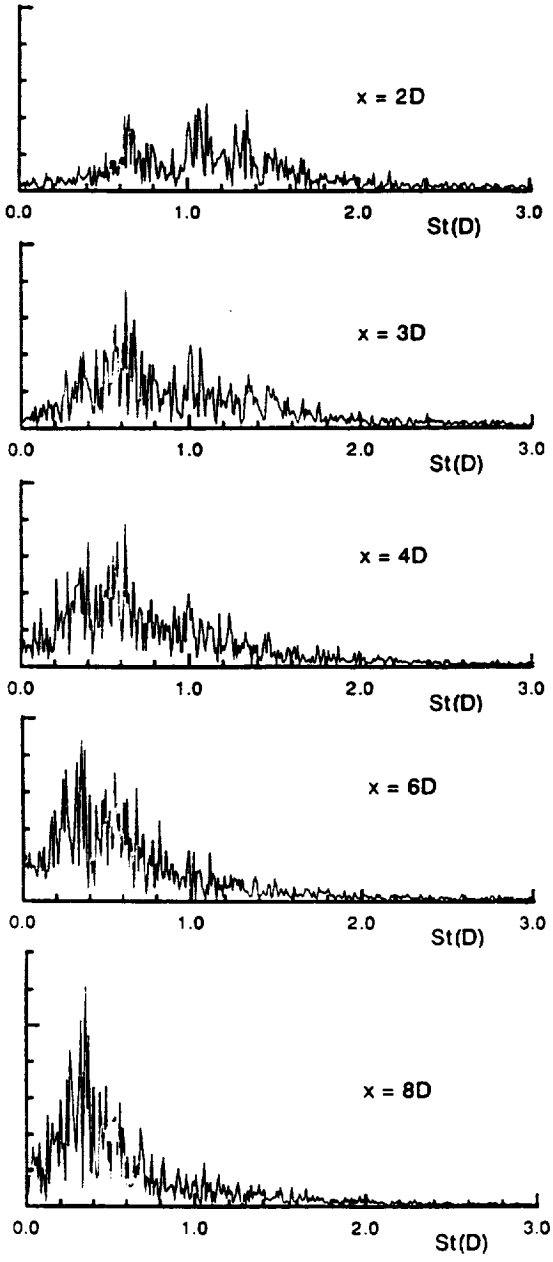

Figure 5. Spectra of the u velocity.

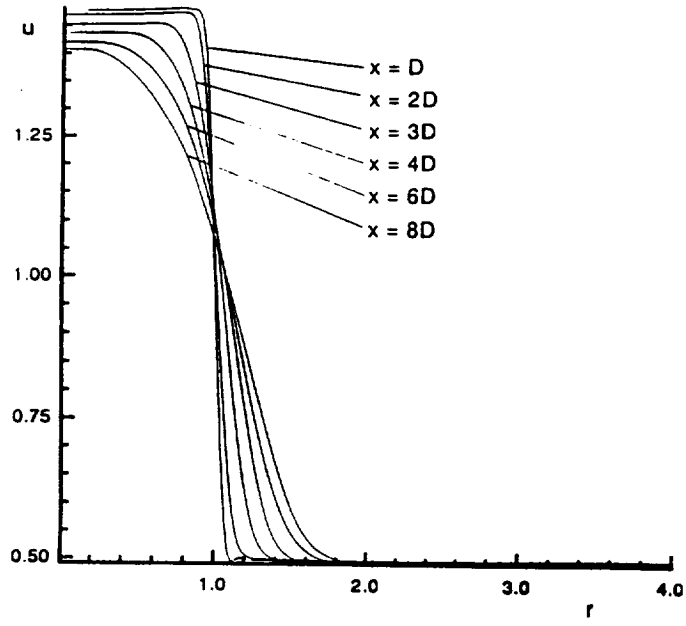

Figure 6. Mean axial velocity.

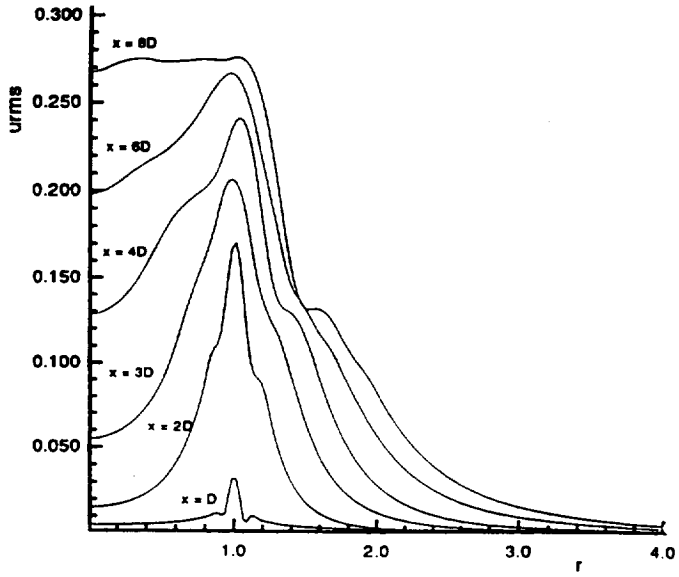

Figure 7. u_{rms} profile.

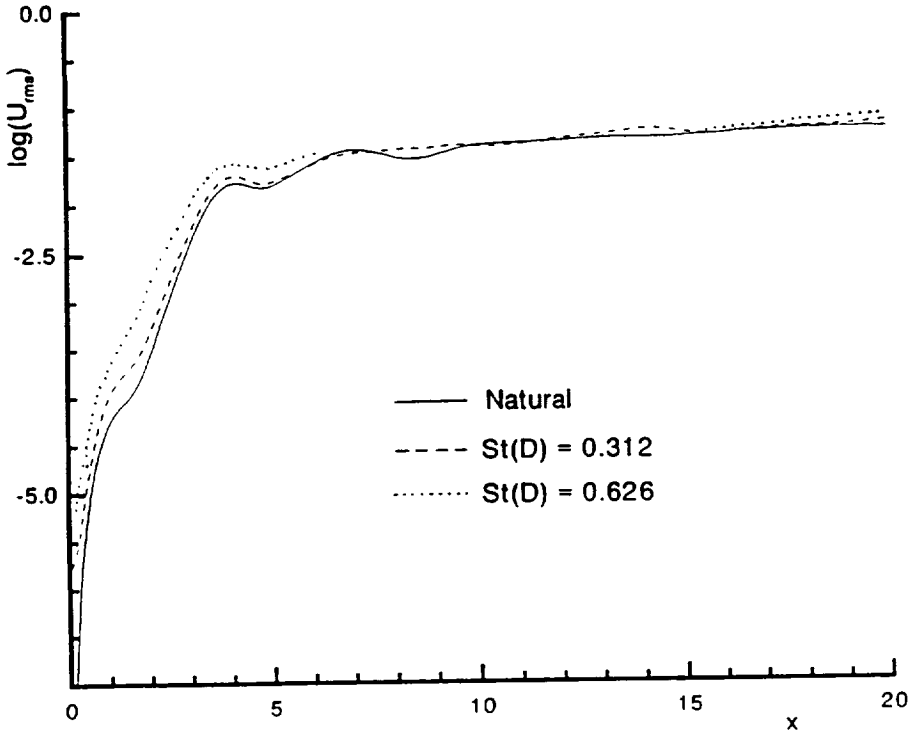

Figure 8. Growth of $u_{\rm rms}$ at r=1 along x.

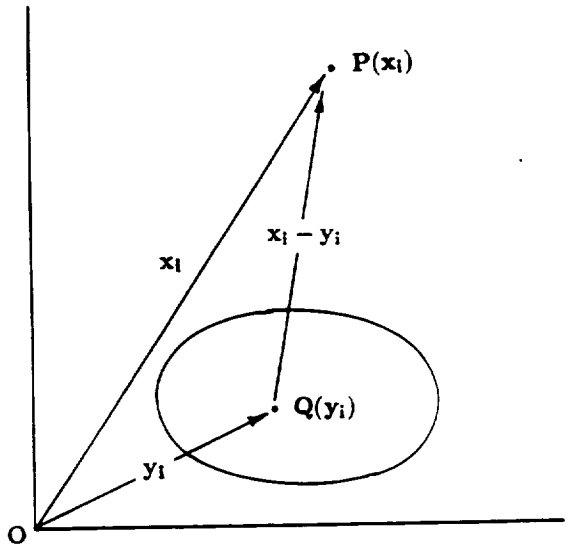

Figure 9-(a). Source and far-field variables in the acoustic analogy.

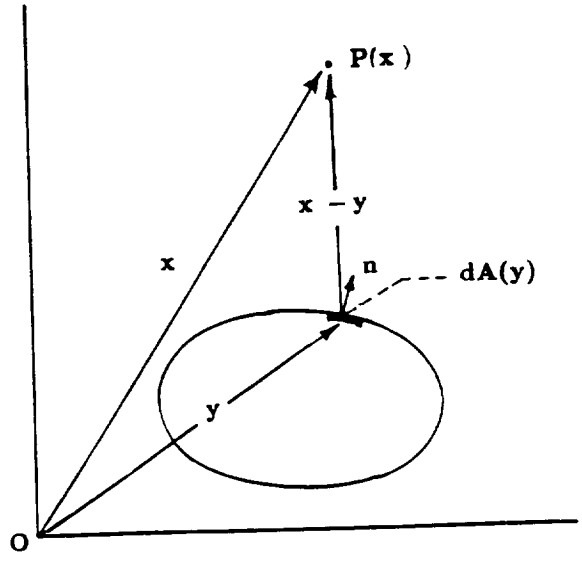

Figure 9-(b). Source and far-field variables in the Kirchhoff surface integral method.

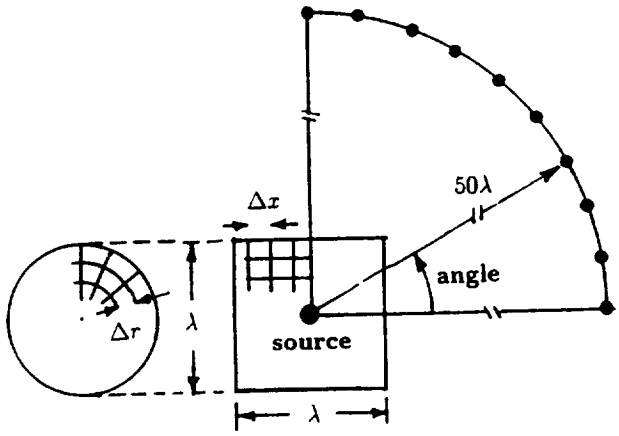

Figure 10. Cylinder surface with a simple source.

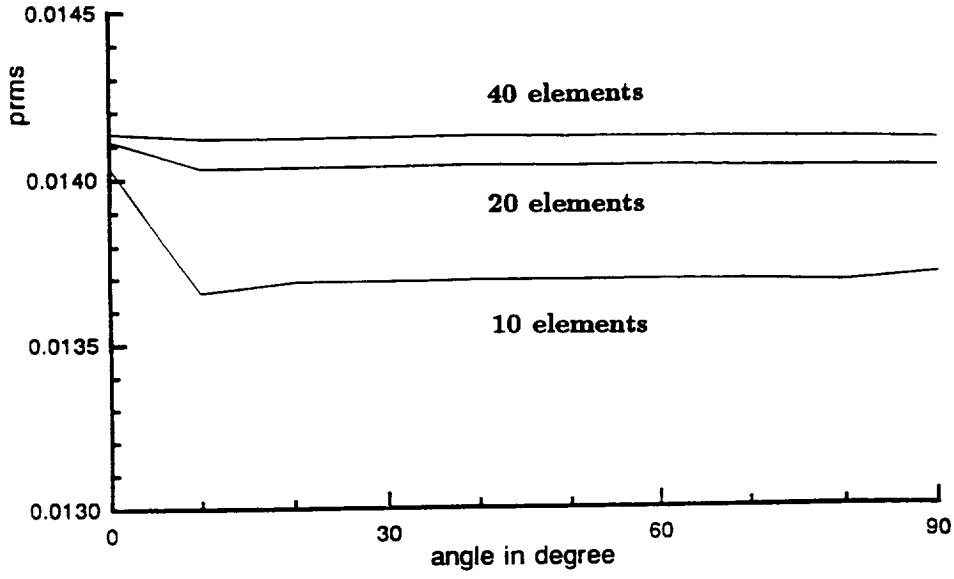

Figure 11. p_{rms} *vs* different time resolutions.

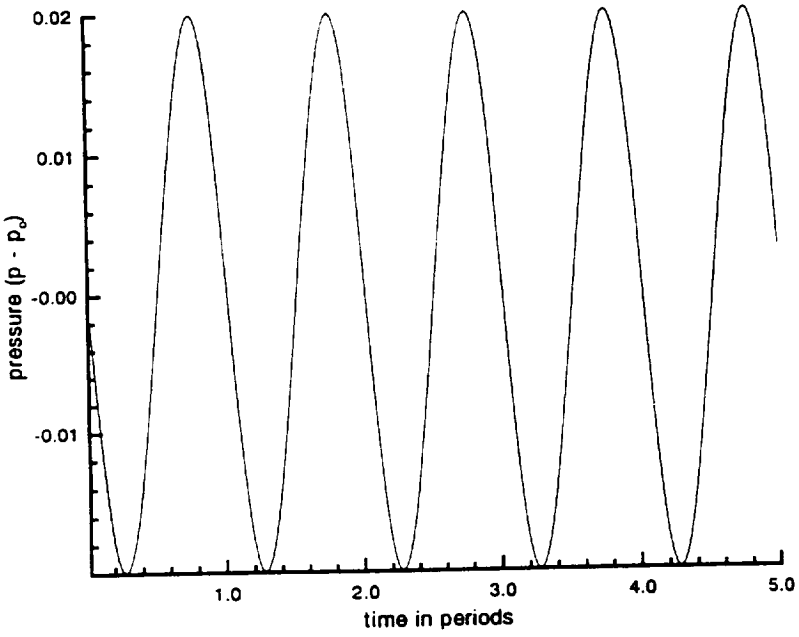

Figure 12-(a). Time history of pressure at r=50

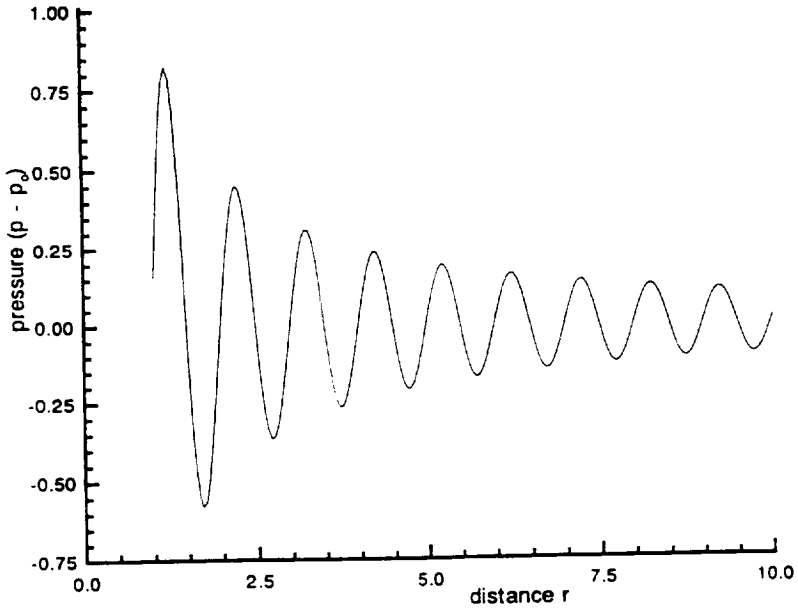

Figure 12-(b). Instantaneous pressure distribution

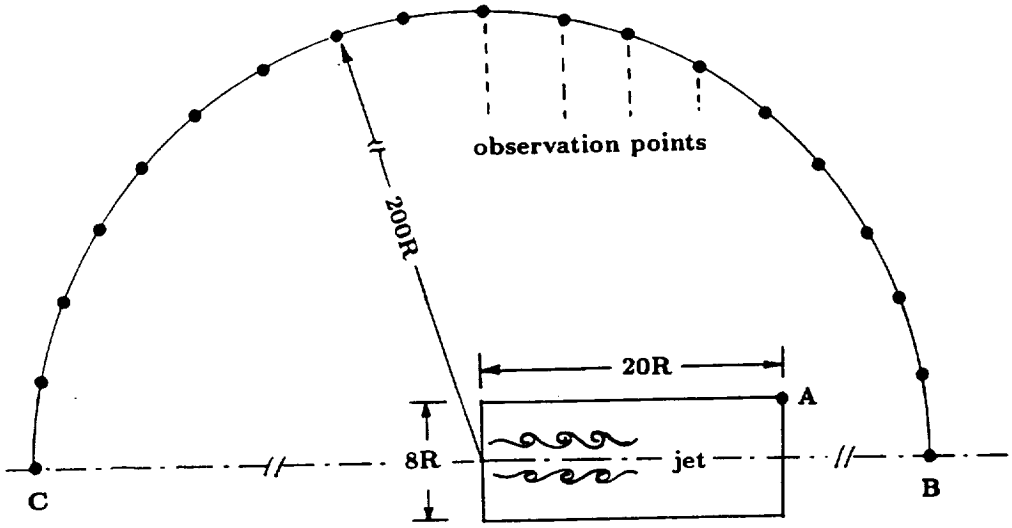

Figure 13. Cylinder surface for the computation of jet noise.

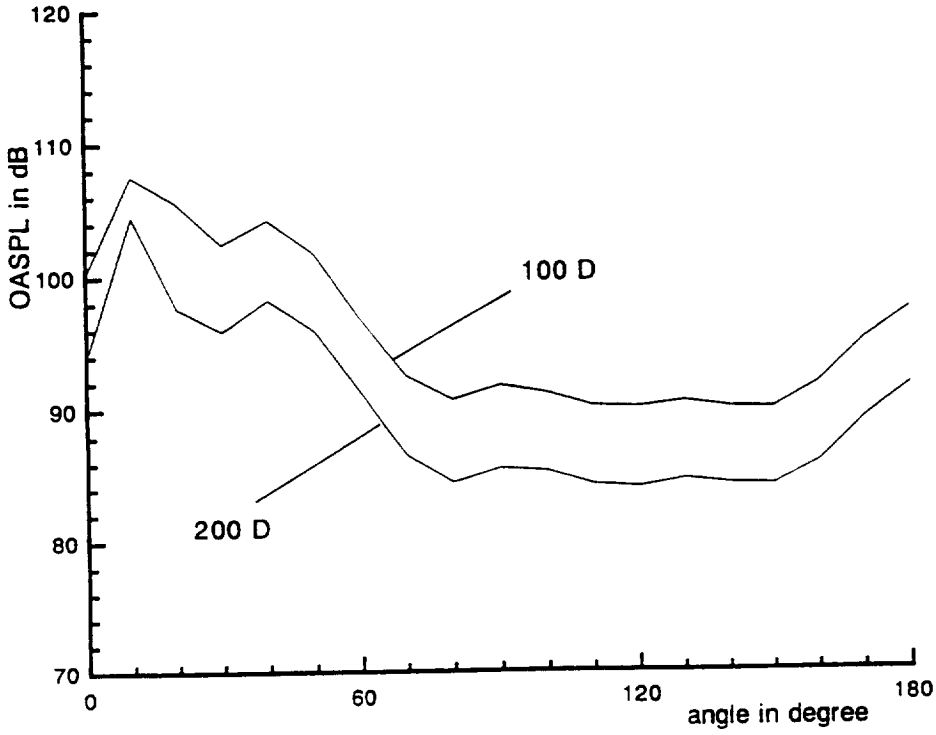

Figure 14. Overall sound pressure level (OASPL) at the distance of $100D$ and $200D$.

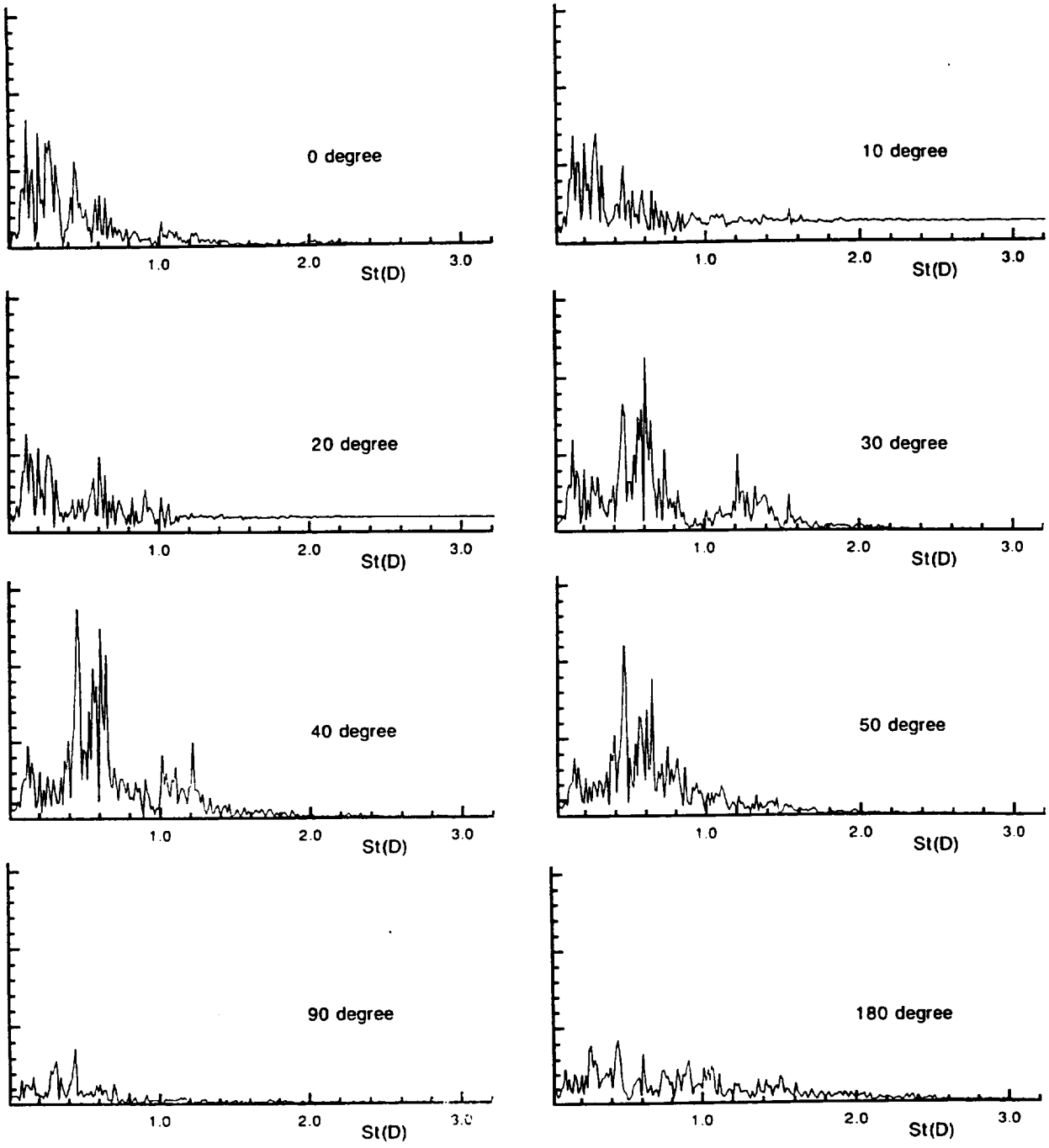

Figure 15. Spectra of the pressure at the distance of $100D$.

REPORT DOCUMENTATION PAGE

Form Approved
OMB No. 0704-0188

1. AGENCY USE ONLY (*Leave blank*)	2. REPORT DATE	3. REPORT TYPE AND DATES COVERED
	January 1994	Final Contractor Report

4. TITLE AND SUBTITLE

Unsteady Jet Flow Computation Towards Noise Prediction

5. FUNDING NUMBERS

WU–537–02–22
C–NAG3–25266

6. AUTHOR(S)

Woo-Yung Soh

7. PERFORMING ORGANIZATION NAME(S) AND ADDRESS(ES)

Sverdrup Technology, Inc.
Lewis Research Center Group
2001 Aerospace Parkway
Brook Park, Ohio 44142

8. PERFORMING ORGANIZATION REPORT NUMBER

E–8329

9. SPONSORING/MONITORING AGENCY NAME(S) AND ADDRESS(ES)

National Aeronautics and Space Administration
Lewis Research Center
Cleveland, Ohio 44135–3191

10. SPONSORING/MONITORING AGENCY REPORT NUMBER

NASA CR–194449
AIAA–94–0138

11. SUPPLEMENTARY NOTES

Prepared for the 32nd Aerospace Sciences Meeting, sponsored by the American Institute of Aeronautics and Astronautics, Reno, Nevada, January 10–13, 1994;(work funded by NASA Contract NAS3–25266). Project Manager, James Scott, Internal Fluid Mechanics Division, (216) 433–5863.

12a. DISTRIBUTION/AVAILABILITY STATEMENT

Unclassified - Unlimited
Subject Category 01

12b. DISTRIBUTION CODE

13. ABSTRACT (*Maximum 200 words*)

An attempt has been made to combine a wave solution method and an unsteady flow computation to produce an integrated aeroacoustic code to predict far-field jet noise. An axisymmetric subsonic jet is considered for this purpose. A fourth order space accurate Pade compact scheme is used for the unsteady Navier-Stokes solution. A Kirchhoff surface integral for the wave equation is employed through the use of an imaginary surface which is a circular cylinder enclosing the jet at a distance. Information such as pressure and its time and normal derivatives is provided on the surface. The sound prediction is performed side by side with the jet flow computation. Retarded time is also taken into consideration since the cylinder body is not acoustically compact. The far-field sound pressure has the directivity and spectra show that low frequency peaks shift toward higher frequency region as the observation angle increases from the jet flow axis.

14. SUBJECT TERMS

Large vortical structure; Sound pressure pade compact scheme; Wave equation

15. NUMBER OF PAGES
17

16. PRICE CODE
A03

17. SECURITY CLASSIFICATION OF REPORT	18. SECURITY CLASSIFICATION OF THIS PAGE	19. SECURITY CLASSIFICATION OF ABSTRACT	20. LIMITATION OF ABSTRACT
Unclassified	Unclassified	Unclassified	